Research Article Vol. 2, No. 9 / 15 September 2019 / OSA Continuum 2496

High-resolution interference microscopy of binary phase diffractive optical elements

MICHAIL SYMEONIDIS,[1,*] WATARU NAKAGAWA,[2] DONG CHEON KIM,[1,3] ANDREAS HERMERSCHMIDT,[3] AND TORALF SCHARF[1]

[1] *Nanophotonics and Metrology Laboratory, École Polytechnique Fédérale de Lausanne (EPFL), 1015 Lausanne, Switzerland*
[2] *Department of Electrical and Computer Engineering, Montana State University, Bozeman, MT 59717-3780, USA*
[3] *HOLOEYE Photonics AG, Volmerstrasse 1, 12489 Berlin, Germany*
[*] *michail.symeonidis@epfl.ch*

Abstract: In this work, we apply the high-resolution interference microscopy technique to investigate the intensity and phase of light transmitted through a binary phase element. Using a combination of simulation and experimental results, we identify specific features in the intensity and phase maps of the transmitted light that are associated with the positions of the edges of the ridges and grooves in the phase element. Specifically, we identify these features to be minima in the intensity recordings, as well as phase jumps and in some cases phase singularities in the phase maps. We focus on the former two features, as they can reliably be observed in a single z-plane intensity or phase image, respectively, focused at the top of the structure ridges. Using the edge locations extracted from the intensity and phase profiles, we estimate the dimensions of the structure ridges and grooves as well as measure the displacement of the sample on a piezo stage. With both methods, the absolute width of the ridges and grooves is measured with an accuracy of approximately 220 nm, and the sample displacement is detected to approximately 50 nm resolution.

1. Introduction

Analysis of the interference pattern of two optical beams is an established method for extracting detailed information about a sample under test (refractive index, thickness, deformation, etc.) [1]. Several methods have been demonstrated to measure surface topography [2], motion [3,4], living tissues [5,6] or to extract three-dimensional data for biological samples [7]. For example, the high-resolution interference microscopy [8] technique has been applied in the metrology field, and has already produced significant results in lens characterization [9,10], the study of focusing effects [11] and amplitude grating investigation [12].

In this work, we apply the high-resolution interference microscope, coupled with a tunable (bandwidth $\approx$ 10 nm) optical source, to investigate the phase features of the light field transmitted through an optical sample. This tool allows us to obtain both the intensity and the phase of the transmitted electric field at a chosen wavelength, thus capturing the full information of the effect that the object has on the transmitted light. This capability is particularly valuable when studying devices that rely on phase for their core functionality, for example diffractive optical elements or phase masks [13]. These devices are being increasingly widely adopted to perform various optical functions, including focusing [14], beam-splitting [15], beam shaping [16], etc. In this work, we study a set of binary phase elements that are designed to induce π phase to the transmitted light at specified positions in the optical aperture, thus realizing the desired optical functionality [17]. Specifically, we present a more complete analysis of the intensity and phase maps taken for this set of devices (building on preliminary work presented in [18]) to investigate small changes in the feature dimensions and lateral position of the sample.

#372671 https://doi.org/10.1364/OSAC.2.002496
Journal © 2019 Received 16 Jul 2019; revised 8 Aug 2019; accepted 8 Aug 2019; published 16 Aug 2019

OSA CONTINUUM

2. High-resolution interference microscope

2.1. Experimental set-up

The aim of this work is to study the intensity and phase profile of light transmitted through a diffractive optical element. The phase regime is not often investigated directly in experiments, due to the increased complexity of the optical set-up needed for this purpose, compared to recording the intensity information only. For example, in most cases magnification beyond the diffraction limit (also called 'empty magnification') does not provide useful information, as the size of a feature projected on the camera is smaller than the point spread function determined by the diffraction-limited optics. However, there are specific points or features in phase measurements that can be localized with high accuracy as they are not subject to the diffraction limit [19], thus taking advantage of the empty magnification.

In our work, we utilize a high-resolution interference microscope to capture both intensity and phase [11,20]. A schematic diagram of the set-up is shown in Fig. 1. The working principle is to incorporate the microscope inside a Mach-Zehnder interferometer, which is a flexible design that can be readily used as a conventional microscope by blocking the reference beam. The interference between the object arm—which carries useful information about the phase profile of the sample—and the reference arm reveals their phase difference, allowing us to record the phase map of the diffracted field. For illumination we use a supercontinuum source (SuperK Fianium, NTK Photonics), which combined with an optical tunable filter (VARIA, NKT Photonics), allows us to carry out measurements at different wavelengths within the visible spectrum. This feature enables the investigation of elements designed to operate at different wavelengths. The passband of the filter has a bandwidth of $BW \approx 10$ nm. An optical delay line, mounted on a precision translation stage (Standa 8MT177-100), is used to minimize the optical path difference between the object and reference arms. The optical path length difference varies for different wavelengths due to the dispersion of the microscope objective and other optical elements. This difference must remain shorter than the coherence length of the source, which is set by the bandwidth of the filter, to have an interference effect. Finally, in order to extract phase information from the interference signal, small phase delays are introduced using a piezo mirror (Mad City Labs, MCL1946) in the reference arm, as is explained in more detail below.

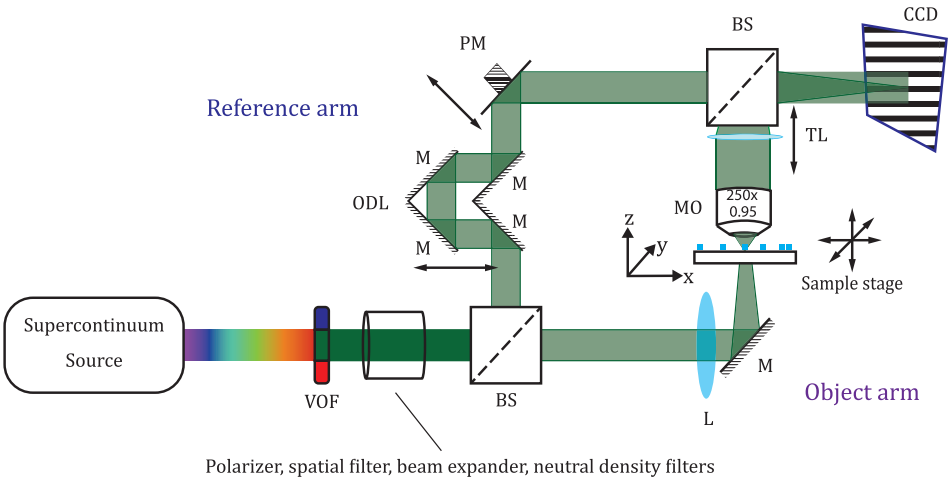

Fig. 1. Schematic diagram of the set-up. The interference microscope is based on the Mach-Zehnder design. VOF: variable optical filter, BS: beam splitter, L: long focal-length lens, M: mirror, MO: microscope objective, ODL: optical delay line, PM: piezo-mirror, CCD: charge-coupled device (camera).

OSA CONTINUUM

An additional piezo stage (Mad City Labs, MSL1945) allows us to make measurements at varying distances from the focal plane of the objective, thus creating a three-dimensional representation of the scattered field. The position of the tube lens, regulated by a precision stage (Standa 8MT177-100), corrects residual wavefront errors of the objective, so that a flat phase profile can be achieved on the CCD camera (Scion Corporation, CFW-1312M, pixel size 4.65 µm×4.65 µm). To ensure the best aberration correction and resolution, we use apochromatic high numerical aperture microscope objectives from Leica, such as the PL APO, 250x / 0.95 objective used in this work. Considering the magnification of this microscope objective and the pixel size of the detector, we estimate that each pixel on the image plane corresponds to PS ≈ 20 nm in both lateral directions, when projected on the object plane. The size of a pixel in the object plane is thus well below the diffraction limited Airy disk radius of 332 nm for a wavelength of $\lambda = 630$ nm. The pixel size correspondance is verified by imaging a sample with known dimensions (Thorlabs R1DS1P, Positive 1951 USAF Test Target).

Given a photo-detector chip-size of ≈ 6 mm, we can image within a field of view of ≈ 20 µm. Due to the small size of the viewing window, the power density throughput of the object arm of the interferometer is low. To compensate for this, we weakly focus the illumination, thus increasing the power density, with a long focal distance lens ($f = 500$ mm). The incoming beam has a diameter of $D \approx 2$ mm, which results in the lens having a numerical aperture of $NA = 2 \times 10^{-3}$ and creates a beam waist of $W \approx 60$ µm (full width at half maximum) at the focal plane. The Rayleigh length of the lens in combination with the fact that the sample lies at its focal plane and the field of view of the objective (20 µm × 25 µm) allow us to assume plane wave illumination.

The high-resolution interference microscope can also be operated as a conventional microscope to record the intensity profile, if the reference arm is blocked. We also perform such intensity measurements in transmission configuration, in order to compare with the phase measurements and set a baseline of operation for our microscope.

2.2. Phase extraction

In order to extract the phase information, we implement the five-step phase shifting technique [1]. The intensity of the interference pattern depends on the power in the two arms and their relative phase difference, which is the quantity of interest. By recording at least three different interferograms, we can determine the pixel-by-pixel phase difference. The piezo mirror changes the optical path of the reference arm by a known amount, changing the phase offset of the reference beam and thus creating a different intensity pattern on the detector. Recording more than three steps makes the algorithm more robust against uncertainties in the induced phase [21]. The five-step implementation is a good compromise between results quality and acquisition time.

3. Sample

3.1. Diffractive optical element

The samples we investigate are binary diffractive optical elements made of fused silica ($n = 1.45$ at $\lambda = 633$ nm). They consists of 20 ridges and grooves, each with a different width, periodically repeated every $\Lambda = 200$ µm. The height of the fused silica ridge is $h \approx 0.7$ µm, thus creating a $\Delta\phi = \pi$ phase difference at the operating wavelength of $\lambda = 633$ nm between the fused silica ridge and the etched groove. A schematic drawing of the sample is shown in Fig. 2.

These elements are fabricated by electron-beam lithography and dry etching to create a chromium etch mask, and then by reactive ion etching to obtain fused silica surface relief phase structures. According to the manufacturer, the variability of the feature widths is expected to be approximately ±100 nm. A series of five devices were produced, each with an incrementally

OSA CONTINUUM

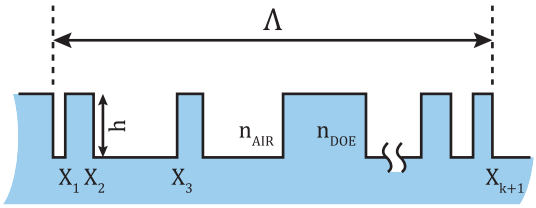

Fig. 2. Schematic diagram of the binary diffractive optical element imaged in this work. It consists of 20 ridges and grooves in a fused silica substrate, yielding a spatially varying phase delay for light propagating through the device. The height of the ridges is $h \approx 0.7$ μm, so as to induce $\Delta\phi = \pi$ phase difference at the operating wavelength of $\lambda = 633$ nm. This pattern is repeated every $\Lambda = 200$ μm. The point X_i corresponds to the position of the i^{th} edge between a ridge and groove.

increasing nominal feature width of $\Delta x = 40$ nm, increasing for the ridge and decreasing for the groove.

3.2. Modeling

In order to understand the expected optical characteristics of this device, we first simulate the electric field transmitted by this structure using a *Rigorous Coupled-Wave Analysis* (RCWA) electromagnetics solver [22–24]. We compute the electromagnetic field diffracted by a phase element with 4 alternating regions of fused silica ($n_{DOE} = 1.4574$ at $\lambda = 633$ nm) and air ($n_{AIR} = 1.0003$ at $\lambda = 633$ nm). The edges of those regions are located at points $X_i = -11.88$ μm, -5.42 μm, 1.92 μm, 4.52 μm and 11.86 μm and the total length of the structure is $l = 23.74$ μm, which corresponds to a portion of the fabricated device. Its height is $h = 0.6924$ μm and 301 Fourier harmonics were used in the simulation. The illumination is taken to be a normally incident plane wave with wavelength $\lambda = 633$ nm. The incident light is polarized at 45° with respect to the x axis, so there is an electric field component both parallel and perpendicular to the groove axis, corresponding to the experimental configuration. The intensity and phase correspond to the vector sum of the two components perpendicular to the propagation direction, $I = |E_x|^2 + |E_y|^2$ and $\Phi = \angle\left\{\frac{1}{\sqrt{2}}(E_x + E_y)\right\}$.

The intensity and phase of the transmitted field immediately after propagation through the device are shown in Figs. 3(a) and 3(b), respectively. For clarity, only the region around a single ridge of width $w = 2.6$ μm is shown. The surface profile of the fused silica substrate and ridge is indicated by the white line. Considering the intensity map shown in Fig. 3(a), we see that there is a null in the intensity above the edges of the ridge. This appears to be the narrowest just above the top of the ridge, as at higher z-positions the interference of various diffraction orders produces a more complex intensity distribution. As will be discussed in more detail below, finding a minimum in an intensity profile measured just above the ridges of the structure enables approximate identification of the location of the edges between the ridges and grooves. Alternatively, the phase map as shown in Fig. 3(b) provides two different methods for identifying these edge positions. The first one relies on the fact that there is a phase jump between the regions above the ridge and above the groove. This characteristic is not surprising, as this device is designed to operate in this fashion. The position where the phase value is equal to the median of the two distinct phase levels gives us an excellent approximation of the actual position of the edges [25–28]. For this method, the results of Fig. 3(b) also suggest that the top surface of the grating ridge might be the best place to observe this phenomenon. Below this level, the phase difference between the light propagating in the ridge and in the groove has not attained its

OSA CONTINUUM

maximum value. Above this height, the phase step gradually blurs, resulting in a less sharply defined phase feature representing the position of the edge.

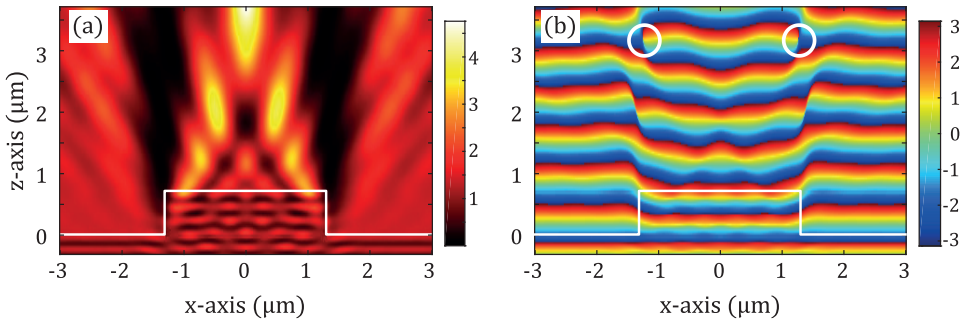

Fig. 3. (a) Intensity and (b) phase results for a region of the simulated structure. The width of the ridge is $W = 2.6$ μm and the illumination wavelength is $\lambda = 633$ nm.

Another possible approach to measure structural details by identifying special phase features is indicated by the white circles drawn on Fig. 3(b), which show the positions of phase singularities. At these points, the diffraction orders interfere destructively, creating a single position where the field is exactly zero [19]. Since there is no amplitude, the phase cannot be defined; these points are commonly called phase singularities or phase residues [29]. In this example, each edge creates a singularity that is sensitive to the polarization of the incoming field. The phase changes by 2π around those points, similar to optical vortices [30]. In order to demonstrate the polarization sensitivity of the phase singularities, we show the phase maps of the transmitted light for a polarization angle of 90° and 50° in Figs. 4(a) and 4(b) respectively. At 90° (electric field perpendicular to the ridge axis y), each edge creates three singularities that are well separated. As the polarization is rotated towards smaller angles (electric field parallel to the ridge), the lower two singularities approach each other, until, around 50° as shown here, almost overlap. When two singularities with opposite signs coincide, they annihilate and they cannot be detected [31]. As the polarization angle becomes even smaller, the condition for the creation of singularity, i.e. destructive interference of the diffraction orders, is satisfied only at higher z axis values, consequently the other singularities cease to exist.

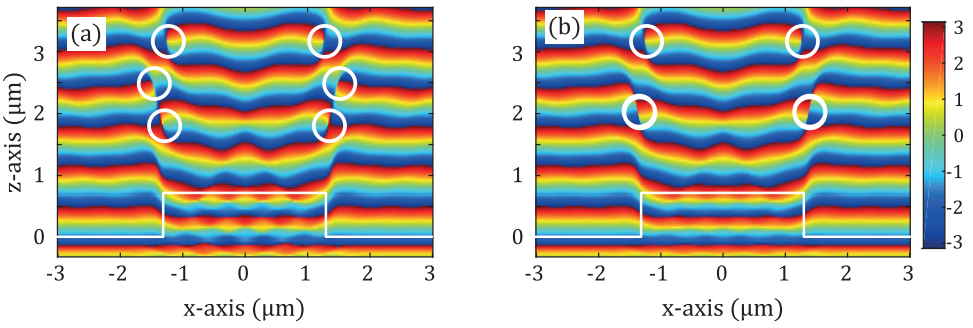

Fig. 4. Phase profiles for incoming polarization at (a) 90° and (b) 50°. The circles indicate the positions of the phase singularities. The white line indicates the position of the phase step.

From these numerical results, we have identified several methods for locating the approximate position of the edges of the the ridge using either the intensity or phase maps. Moreover, these

OSA CONTINUUM

characteristics are likely to be particularly pronounced with this structure, as it is engineered to have a $\Delta\phi = \pi$ phase difference. However, since the incident light is polarized at 45°, the detection of singularities requires longer measurements along the z-axis, which increases both the recording and processing time. Consequently, in Section 4, we choose to focus on measurements that are taken in a single plane. An example profile of the intensity and phase from the simulation data presented in Fig. 3 at $z = 0.7$ µm—at the top of the ridge—is shown in Fig. 5.

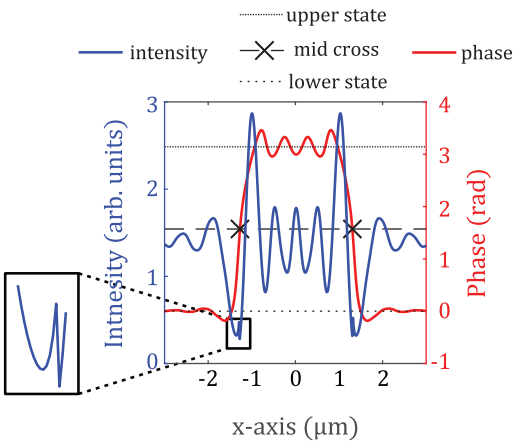

Fig. 5. Simulated intensity (blue) and phase (red) profiles at $z = 0.7$ µm for wavelength $\lambda = 633$ nm. Both the minimum in the intensity profile and the middle-crossing point in phase profile localize the edge with an accuracy of +10 nm to −30 nm. The inset shows a detailed view of the intensity profile that cannot be resolved by the optical system.

As can be seen in Fig. 5, both the lateral position of the minimum in an intensity profile or the phase jump in a phase profile are suitable to identify the location of the edges between the ridges and grooves of this structure, with an accuracy of +10 nm to −30 nm. The inset shows the fine details of the intensity profile, which in principle could improve accuracy, but that cannot be resolved by the optical system. Although the middle-crossing underestimates the width by 20 nm and the intensity minimum by 10 nm, the values are still within the expected experimental accuracy. As described above, the simulation results suggest that observing either the intensity or phase profile in a plane aligned with the top surface of the ridges is likely to facilitate detection of the structure edges. Thus, we conclude that locating the minima in an intensity profile or the jumps in a phase profile taken just above the surface of the structure are both appropriate methods to approximately identify the locations of the edges of the ridges on this structure.

3.3. *Preliminary measurements*

To compare with the simulation results, we first perform a three-dimensional scan of a corresponding region of the sample. Images of a ridge with nominal width $w = 2.6$ µm are taken. The sample is then translated along the z-axis (propagation direction), with a step of 65 nm and 33 nm for the intensity and phase, respectively. At each position we record both quantities and subsequently, we create the three dimensional representation of the field by stacking the recorded slices on top of each other. The results of the measurements are shown in Figs. 6(a) and 6(b) for intensity and phase, respectively. The cross-sections are averaged over 10 slices of the $x - z$ plane to reduce the noise, corresponding to $\approx$ 190 nm along y-axis (the structure is invariant along this direction). The solid white line represents the surface of the fused silica substrate and ridge.

Comparing Figs. 3 and 6, we see that the experimental measurements agree very well with the simulations in the air region above the structure. Most pertinent to this work are the dark

OSA CONTINUUM

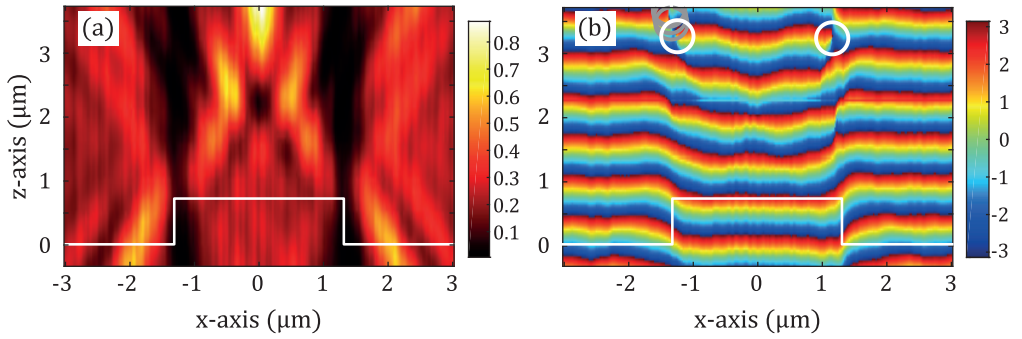

Fig. 6. Measurement of (a) intensity and (b) phase maps as measured using the high-resolution interference microscope to image a section of the diffractive optical element with illumination at 633 nm. An average of 10 slices of the $x - z$ plane is presented. The white line represents the surface of the fused silica substrate and ridge. The circles indicate the position of the phase singularities.

bands in the intensity map located above the edges of the ridge, and the phase steps in the phase maps also located above the edges of the ridge. The experimental set-up also captures the predicted phase singularities (indicated by white circles), as well as some additional ones (indicated by gray circles). These singularities, while not seen in the simulation results, are not entirely unexpected, as the intensity of the field is very low in that region. This result, along with any slight deviation of the measurement from the simulation (e.g. differences in singularity positions), is understandable since the microscope objective cannot capture all of the spatial frequencies, as is the case in the simulation. Moreover, the simulations were carried out with a strictly monochromatic illumination, while the measurements were performed with an illumination bandwidth of $\approx$ 10 nm. Inside the fused silica region (below the white line in Fig. 6), the simulation and experimental results differ significantly. In the simulation results, it is possible to compute the field intensity and phase exactly, whereas in the experimental results, we shift the focal plane of the microscope below the material interface, but must still image through the non-flat surface of the sample. Evidently, the instrument is unable to effectively image below the structured surface of the sample. In the following, we will only consider intensity and phase maps taken at or above the surface of the sample.

We can now proceed to determine the ridge and groove (not shown) widths using both the intensity and phase maps for each z plane shown in Fig. 6 as a function of the focal plane position. These results are shown in Figs. 7(a) and 7(b), for the measured width of the ridge and groove, respectively, using the intensity (blue) and phase (red) data. As shown in Fig. 7, the intensity and phase results are close when the top surface of the ridge is in focus (height = 0.7 μm). The phase profile is more sensitive to defocusing; nevertheless, close to the focal plane (±100 nm), the deviation is smaller than 50 nm. We note that this agreement may be a result of the specific characteristics of the devices under study, and not necessarily generally applicable. However, this result is also consistent with the expectations set by the simulation results described previously. Thus, for this sample, we conclude that if we wish to record a two-dimensional image in a single z plane, we will attempt to position the focal plane of the imaging system at the surface of the ridges in the sample.

OSA CONTINUUM

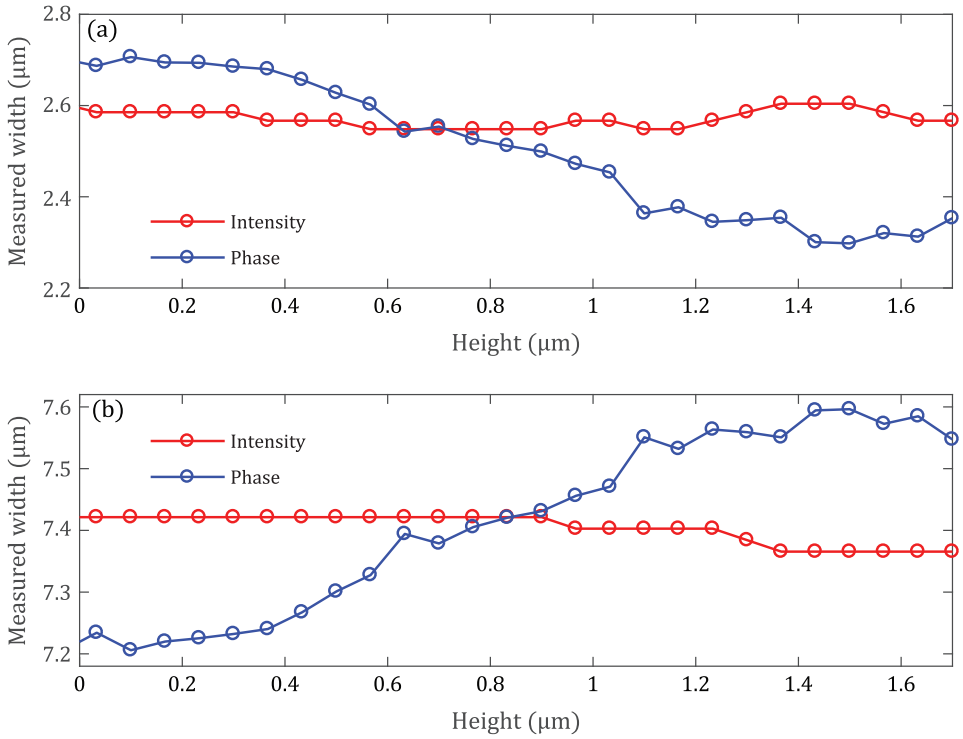

Fig. 7. Measured width of the (a) ridge and (b) groove as a function of the focal position. The results agree near the top surface of the ridge.

4. Measurement results

We now investigate the use of the instrument and methodology to characterize the size and position of the ridge and groove features. Both methods, utilizing the intensity and phase profiles extracted from images taken at a single z-plane located at the surface of the sample, are explored. The experimental conditions under which each measurement was taken, were kept the same (power impinging on the sample, gain and integration time of the detector), to ensure a fair comparison between them.

4.1. Image acquisition and processing

In order to extract only the intensity and phase changes that the sample induces in the incoming field, we remove the unwanted background signal by post-processing the data. For the intensity, we first record the intensity profiles with the sample mounted and normalize every image to its mean value. Figure 8(a) shows a normalized image of the sample, where a gradient in the illumination field is observed. Next, we record and normalize a background image, without the sample, as shown in Fig. 8(b), where the same gradient is present. Taking the difference of the two images, shown in Fig. 8(c), produces a more uniform image where the features of the sample are more clearly visible.

The process for the phase is similar. We first record the five intensity images to extract the phase map of the transmitted field through the sample and unwrap it. Figure 8(d) shows the unwrapped phase map of an example measurement, where phase variations in regions where the phase should be constant are observed. Next we extract and unwrap the phase map of the background (no sample), as shown in Fig. 8(e). From this image we see that the variations

OSA CONTINUUM

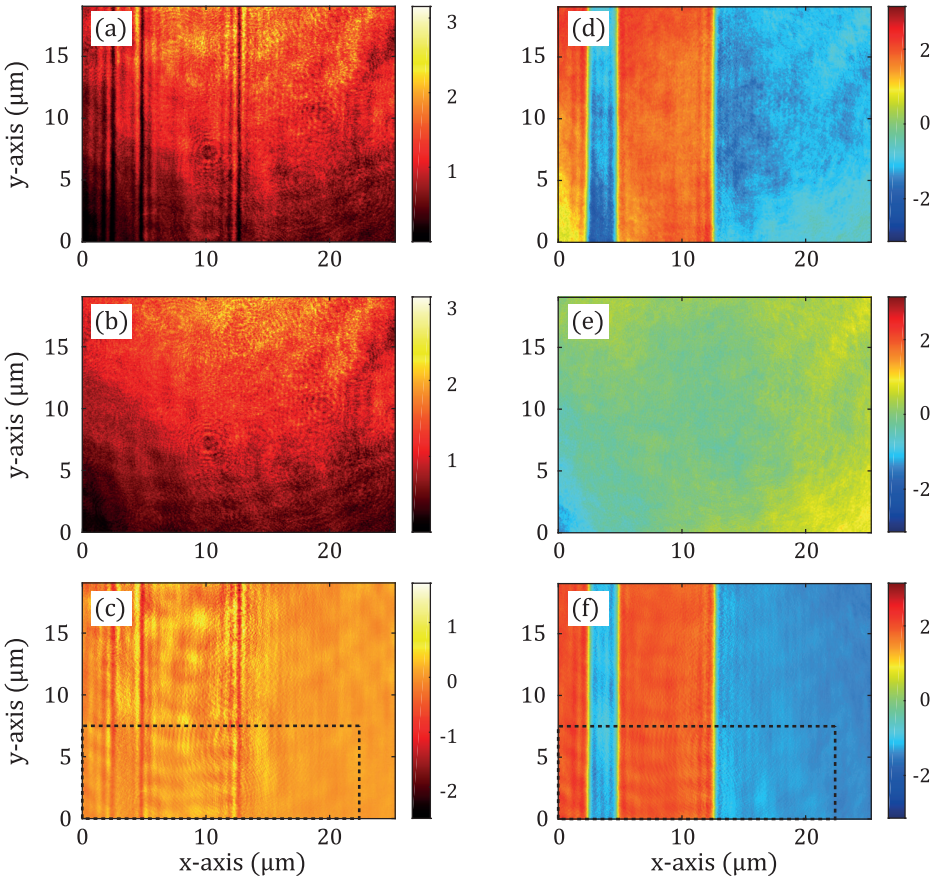

Fig. 8. (a) Normalized intensity image of the sample, (b) normalized intensity image of the background and (c) their difference. (d) unwrapped phase map of the sample, (e) unwrapped phase map of the background, and (f) their difference after phase re-wrapping. The dashed rectangles in (c) and (f) indicate the area plotting in Fig. 9.

observed earlier are also visible in the background. Finally, we subtract these two images and re-wrap the phase difference in the $(-\pi, \pi]$ interval. The result is shown in Fig. 8(f), which is again more uniform and highlights the features of the sample. This procedure suppresses any bias or systematic error that comes from the set-up itself, such as a differential response of the pixels in the detector or deviations from a plane wavefront in the incident illumination.

4.2. Profile extraction

Figures 9(a) and 9(b) show a region of the maps in intensity and phase, respectively, presented in Figs. 8(c) and 8(f) (as indicated by the dashed rectangles). Figures 9(c) and 9(d) show the intensity and phase profiles, respectively, averaged along the groove axis, y. Averaging over a number of lines in the image mitigates the effects of noise. Based on the simulation results described in Section 3, we observe the expected minima in the intensity profile in Fig. 9(c), as well as the expected steps in the phase profile of Fig. 9(d). In addition, as expected, the phase difference in the phase steps is within $\pm 1\%$ of π.

The minima in intensity, indicated by the magenta asterisks in Fig. 9(c) are found by simply finding the location of the minimum value, around the expected position of the edge. For the middle-values localization in the phase profiles, indicated by the blue x'es, the function

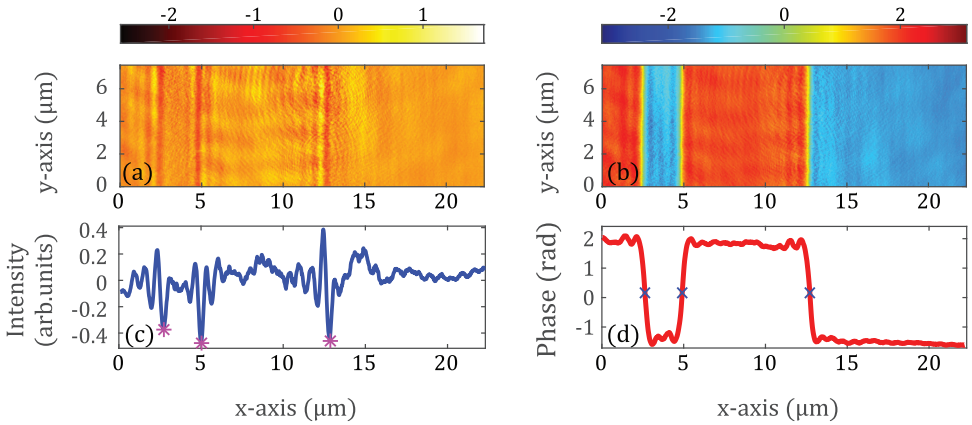

Fig. 9. (a) Intensity and (b) phase images of a region of the sample (indicated by the dashed rectangles in Figs. 8(c) and 8(f), respectively). (c), (d): Averaged profiles along 400 lines of the *y*-axis for the intensity and phase maps, respectively.

`midcross` of *Matlab* was used. Using those points, we measure the width of the ridge to be 2.31 μm / 2.30 μm and of the groove 7.89 μm / 7.86 μm for intensity and phase respectively, compared to the nominal values of 2.44 μm and 7.50 μm.

4.3. Feature size determination

The positions of the edges of the ridges and grooves are determined using the methods described above, namely by locating the positions of the minima in the intensity profiles and by finding the middle-crossing points in the phase profiles. Here, we image a region of the sample containing one ridge and one groove, and estimate the width of each feature. This measurement is repeated five times on different samples with a slightly different ridge and groove width, as described in Section 3. The nominal widths of each feature for the five samples are shown in Tables 1 and 2. The measured intensity and phase profiles for the five structures, averaged over 500 lines from the original image, are shown in Fig. 10. For each profile, the distance between adjacent points of interest (minima/phase jumps) is computed, approximating the width of each ridge or groove. These results are also presented in Tables 1 and 2.

Table 1. Nominal and measured widths of device ridges

		Width – Ridge(μm)			
		(*Intensity*)		(*Phase*)	
Sample	*Nominal*	*Measured*	*Difference*	*Measured*	*Difference*
1	2.44	2.66	0.22	2.58	0.14
2	2.48	2.70	0.22	2.62	0.14
3	2.52	2.72	0.20	2.63	0.11
4	2.56	2.77	0.21	2.70	0.14
5	2.60	2.81	0.21	2.77	0.17

Both methods, using the intensity and phase images, yield width values for the ridges which are slightly higher than the nominal values, and widths for the grooves which are slightly lower. However, all of the measured widths are within approximately 0.22 μm of the nominal values. In addition, the positions determined by the two methods agree to within approximately the

OSA CONTINUUM

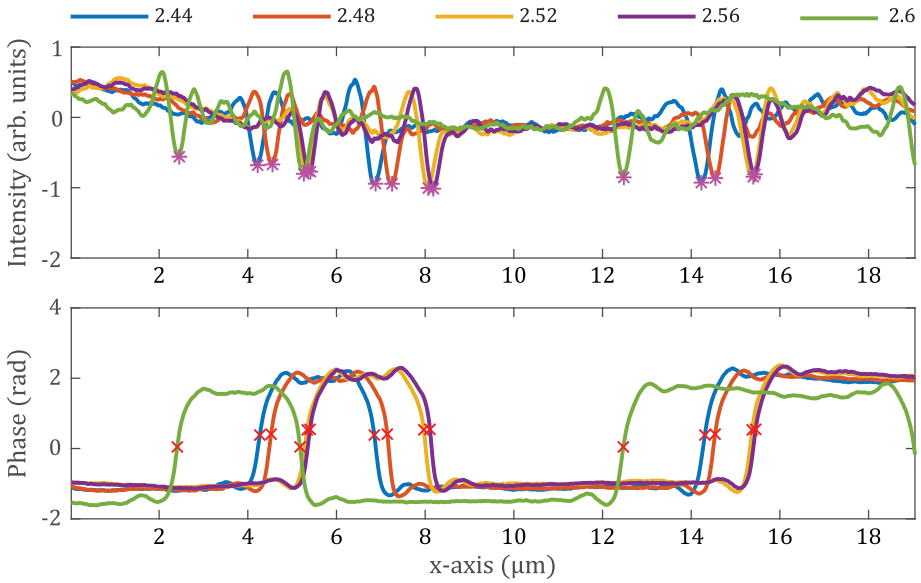

Fig. 10. (top) Intensity and (bottom) phase profiles of the five measured structures. Edges between ridges and grooves are observed as minima in the intensity profiles (indicated by magenta asterisks), and as jumps in the phase profiles (indicated by red x'es).

Table 2. Nominal and measured widths of device grooves

		Width – Groove(μm)			
		(*Intensity*)		(*Phase*)	
Sample	*Nominal*	*Measured*	*Difference*	*Measured*	*Difference*
1	7.50	7.35	−0.15	7.46	−0.04
2	7.46	7.29	−0.17	7.39	−0.07
3	7.42	7.33	−0.09	7.41	−0.01
4	7.38	7.25	−0.13	7.35	−0.03
5	7.34	7.22	−0.12	7.29	−0.05

tolerance stated above. Moreover, in most cases the width values found using the phase images are slightly closer to the nominal values than those using the intensity images.

4.4. Displacement

Next, we observe the position of the sample feature edges after laterally translating the sample by a known amount. To achieve this, the sample was mounted on a piezo stage (PI P-517.3CL, movement precision 1 nm) that translated the sample along the x-direction relative to the first measurement (denoted as displacement 0 μm). After each translation step, the intensity and phase profiles were recorded and the exact displacement was verified by the sensor of the piezo stage, which is used in closed-loop operation. Along the y (invariant) direction, 800 rows of the image are averaged to produce the intensity and phase measurement profiles shown in Figs. 11(a) and 11(b), respectively. In the intensity profiles, the edges between ridges and grooves are associated with intensity minima. The positions of these minima are found, and indicated by magenta asterisks in Fig. 11(a). For each profile, a total of three minima are identified, corresponding to the three edges in the original image. The displacement of each edge relative to the first measurement are computed, and the average displacement for each case is shown in Table 3. For

OSA CONTINUUM

the phase profiles, the positions of the edges are associated with phase jumps. The mid-point of each such phase jump is observed, as indicated by the red x'es in Fig. 11(b). The displacement of each of the three edges is computed, and averaged as also shown in Table 3.

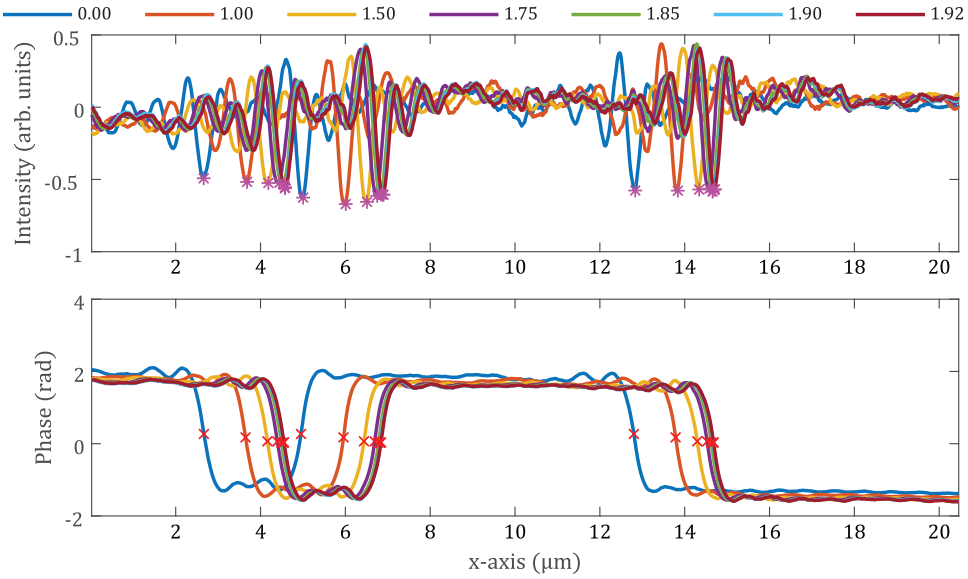

Fig. 11. (top) Intensity and (bottom) phase profiles averaged over 800 lines of the captured image, for seven different translational positions along the x-axis, as indicated in the legend (in μm). Edges between ridges and grooves are observed as minima in the intensity profiles (indicated by magenta asterisks), and as jumps in the phase profiles (indicated by red x'es).

Table 3. Measured and nominal edge displacement

	Nominal Displacement (μm)					
	1.00	1.50	1.75	1.85	1.90	1.92
Intensity						
Displacement(μm)	1.01	1.51	1.76	1.85	1.88	1.90
Offset(nm)	11	13	11	4	−15	−23
Deviation(%)	1.06	0.85	0.62	0.21	0.80	1.19
Phase						
Displacement(μm)	0.99	1.49	1.73	1.83	1.87	1.88
Offset(nm)	−10	−8	−18	−23	−26	−36
Deviation(%)	1.04	0.51	1.04	1.25	1.35	1.87

In addition to the displacements measured using both the intensity image and the phase image, Table 3 also shows the offset (in nm) of each measurement, as well as the percentage deviation from the nominal value. Of note is the fact that each measurement is within approximately 50 nm or 2.5% of the nominal displacement value. Comparing the two methods, the positions of the edges are found to agree within the tolerance of approximately 50 nm, although the intensity image seems to provide a slightly lower deviation than the phase image in most cases shown. However, the method used in analyzing the intensity images incorporates a peculiarity of a binary diffractive optical element, where a phase change of π is expected between a ridge and groove. In cases where exact destructive interference might not be expected at such an edge, the phase image

OSA CONTINUUM

may prove to be more reliable. In addition, this experiment can in some ways be considered to be a differential measurement, as the same features are measured, then displaced by a small known distance, and then measured again, eliminating some possible sources of uncertainty (e.g. fabrication imperfections). More broadly, comparing Figs. 11(a) and 11(b), we can see that the phase approach provides a more distinct indication of the feature edges, and thus might be expected to be more tolerant to noise. Finally, while admittedly referring to a single set of samples with a known profile and desirable characteristics such as a π phase step between ridges and grooves, under these conditions analysis of both the intensity and phase measurements is able to observe and quantify translational displacements of the sample with sensitivity on the order of 50 nm, well below the classical diffraction limit.

5. Conclusion

In this work we record the intensity and phase maps of the light transmitted through a binary phase element that is designed to induce a π phase delay between its ridges and grooves. This phase difference creates specific features in both the intensity and phase profiles, which we use to localize the position of the edges of the ridges and grooves. More specifically, using both numerical and experimental results, we show that the minima in the intensity profiles and jumps in the phase profiles approximately indicate the positions of these edges. We also observe experimentally phase singularities that provide a possible alternative method for edge localization, although they require three-dimensional scanning measurements. Based on the experimental and simulation results for this particular device (having a π phase step when operated at the design wavelength of $\lambda = 633$ nm), we determine that an image taken in a single z-plane located at the top of the ridges (i.e. at the upper surface of the structure) can provide useful information about the position of the feature edges using either the intensity or phase methods. We note that in this study the intensity and phase methods perform approximately equivalently, likely due to the fact that the phase delay in this element is exactly π radians.

From the position of the edges, we calculate the widths of the material ridges and grooves, as well as track the displacement of the structure. Using this method, we estimate the dimensions of the structure with an accuracy of approximately 220 nm and we measure sample displacements as small as about 50 nm. Comparing the two methods—intensity and phase—for this specific sample and with this instrument, we find that both approaches are approximately equivalent in terms of resolution. It is likely, however, that the π phase step found in this device makes the intensity contrast at the feature edges particularly stark due to destructive interference. We expect that for devices with different or multiple phase steps, the phase mapping method would be more robust and better able to image the feature edges within such a device.

Also, in this work we illuminate at the intended wavelength of operation of the device, namely $\lambda = 633$ nm. However, the instrument is able to operate at a range of optical wavelengths, facilitating the investigation of optical phenomena such as phase singularities, as well as permitting the characterization of samples designed to operate at other wavelengths. In addition, this instrument is able to capture both conventional and interferometric (phase-resolved) images, facilitating the characterization of a broad range of optical samples, in particular those for which phase plays an important role in their functionality. For example, although further investigation would be needed, these results suggest that this instrument and approach might have applications in metrology and quality control of diffractive optical elements.

Funding

Schweizerischer Nationalfonds zur Förderung der Wissenschaftlichen Forschung (513699); H2020 Marie Skłodowska-Curie Actions (675745).

OSA CONTINUUM

Acknowledgments

The authors gratefully acknowledge J. P. Hugonin and P. Lalanne, Institute d' Optique, Orsay, France, for providing freely the *Reticolo software for grating analysis* (2005). This project has received funding from the European Union's Horizon 2020 research and innovation program under the Marie Skłodowska-Curie grant agreement no. 675745.

References

1. E. P. Goodwin and J. C. Wyant, *Field Guide to Interferometric Optical Testing* (SPIE Field Guides SPIE, 2006).
2. P. de Groot, "Principles of interference microscopy for the measurement of surface topography," Adv. Opt. Photonics **7**(1), 1 (2015).
3. W. Hemmert, M. S. Mermelstein, and D. M. Freeman, "Nanometer resolution of three-dimensional motions using video interference microscopy," in *Technical Digest. IEEE International MEMS 99 Conference. Twelfth IEEE International Conference on Micro Electro Mechanical Systems (Cat. No.99CH36291)* (1999), pp. 302–308.
4. C. Fang-Yen, S. Oh, Y. Park, W. Choi, S. Song, H. S. Seung, R. R. Dasari, and M. S. Feld, "Imaging voltage-dependent cell motions with heterodyne Mach-Zehnder phase microscopy," Opt. Lett. **32**(11), 1572–1574 (2007).
5. A. Dubois, L. Vabre, A.-C. Boccara, and E. Beaurepaire, "High-resolution full-field optical coherence tomography with a Linnik microscope," Appl. Opt. **41**(4), 805–812 (2002).
6. M. Mihailescu, M. Scarlat, A. Gheorghiu, J. Costescu, M. Kusko, I. A. Paun, and E. Scarlat, "Automated imaging, identification, and counting of similar cells from digital hologram reconstructions," Appl. Opt. **50**(20), 3589–3597 (2011).
7. W. Choi, "Tomographic phase microscopy and its biological applications," 3D Res. **3**(4), 5 (2012).
8. C. Rockstuhl, I. Marki, T. Scharf, M. Salt, H. Peter Herzig, and R. Dändliker, "High resolution interference microscopy: a tool for probing optical waves in the far-field on a nanometric length scale," Curr. Nanosci. **2**(4), 337–350 (2006).
9. M.-S. Kim, T. Scharf, and H. P. Herzig, "Small-size microlens characterization by multiwavelength high-resolution interference microscopy," Opt. Express **18**(14), 14319–14329 (2010).
10. M.-S. Kim, T. Scharf, S. Mühlig, M. Fruhnert, C. Rockstuhl, R. Bitterli, W. Noell, R. Voelkel, and H. P. Herzig, "Refraction limit of miniaturized optical systems: a ball-lens example," Opt. Express **24**(7), 6996–7005 (2016).
11. M.-S. Kim, T. Scharf, S. Mühlig, C. Rockstuhl, and H. P. Herzig, "Gouy phase anomaly in photonic nanojets," Appl. Phys. Lett. **98**(19), 191114 (2011).
12. M.-S. Kim, T. Scharf, C. Menzel, C. Rockstuhl, and H. P. Herzig, "Talbot images of wavelength-scale amplitude gratings," Opt. Express **20**(5), 4903–4920 (2012).
13. V. Katkovnik, M. Ponomarenko, and K. Egiazarian, "Lensless broadband diffractive imaging with improved depth of focus: wavefront modulation by multilevel phase masks," J. Mod. Opt. **66**(3), 335–352 (2019).
14. M. B. Fleming and M. C. Hutley, "Blazed diffractive optics," Appl. Opt. **36**(20), 4635–4643 (1997).
15. A. Sabatyan and B. Fathi, "High-efficiency arrays of any desired optical beams using modified grating-based elements," Opt. Quantum Electron. **50**(9), 338 (2018).
16. L. G. Neto, P. S. P. Cardona, G. A. Cirino, R. D. Mansano, and P. B. Verdonck, "Design, fabrication, and characterization of a full complex-amplitude modulation diffractive optical element," J. Micro/Nanolith. MEMS MOEMS **2**(2), 96–104 (2003).
17. Y. G. Soskind, *Field Guide to Diffractive Optics*, vol. FG21 of *SPIE Field Guides* (SPIE, 2011).
18. M. Symeonidis, D. C. Kim, A. Hermerschmidt, M.-S. Kim, and S. Toralf, "Diffractive optical elements investigation in the phase domain," Proc. SPIE **10914**, 72 (2019).
19. C. Rockstuhl, M. Salt, and H. P. Herzig, "Theoretical and experimental investigation of phase singularities generated by optical micro- and nano-structures," J. Opt. A: Pure Appl. Opt. **6**(5), S271–S276 (2004).
20. M.-S. Kim, T. Scharf, S. Muhlig, C. Rockstuhl, and H. P. Herzig, "Engineering photonic nanojets," Opt. Express **19**(11), 10206–10220 (2011).
21. P. Hariharan, B. F. Oreb, and T. Eiju, "Digital phase-shifting interferometry: a simple error-compensating phase calculation algorithm," Appl. Opt. **26**(13), 2504–2506 (1987).
22. M. G. Moharam, E. B. Grann, D. A. Pommet, and T. K. Gaylord, "Formulation for stable and efficient implementation of the rigorous coupled-wave analysis of binary gratings," J. Opt. Soc. Am. A **12**(5), 1068–1076 (1995).
23. P. Lalanne and G. M. Morris, "Highly improved convergence of the coupled-wave method for TM polarization," J. Opt. Soc. Am. A **13**(4), 779–784 (1996).
24. P. Lalanne and M. P. Jurek, "Computation of the near-field pattern with the coupled-wave method for transverse magnetic polarization," J. Mod. Opt. **45**(7), 1357–1374 (1998).
25. E. Cuche, F. Bevilacqua, and C. Depeursinge, "Digital holography for quantitative phase-contrast imaging," Opt. Lett. **24**(5), 291–293 (1999).
26. C. J. Mann, L. Yu, C.-M. Lo, and M. K. Kim, "High-resolution quantitative phase-contrast microscopy by digital holography," Opt. Express **13**(22), 8693–8698 (2005).
27. S. Lee, J. Y. Lee, W. Yang, and D. Y. Kim, "Autofocusing and edge detection schemes in cell volume measurements with quantitative phase microscopy," Opt. Express **17**(8), 6476–6486 (2009).

OSA CONTINUUM

28. P. Lehmann, J. Niehues, and S. Tereschenko, "3-D Optical Interference Microscopy at the Lateral Resolution," Int. J. Optomechatronics **8**(4), 231–241 (2014).
29. V. P. Tychinsky, "Superresolution and singularities in phase images," Phys.-Usp. **51**(11), 1161–1169 (2008).
30. G. J. Gbur, *Singular Optics*, Series in optics and optoelectronics (Taylor & Francis, 2017).
31. M. R. Dennis, K. O'Holleran, and M. J. Padgett, "Chapter 5 Singular Optics: Optical Vortices and Polarization Singularities," in *Progress in Optics*, vol. 53 E. Wolf, ed. (Elsevier, 2009), pp. 293–363